# *Ab initio* modeling of diffusion in indium oxide

Péter Ágoston[*] and Karsten Albe

*Institut für Materialwissenschaft, Technische Universität Darmstadt, Petersenstr. 32, D-64287 Darmstadt, Germany*

(Received 20 August 2009; revised manuscript received 14 March 2010; published 7 May 2010)

Migration barriers of intrinsic defects in cubic indium oxide are calculated by means of first-principles calculations within density-functional theory using the nudged-elastic-band method. Within the open C-type (bixbyite) structure of $In_2O_3$ there is a large variety of distinct migration paths involving the fourth-neighbor shell. Effective migration energies and diffusion length are calculated by means of kinetic Monte Carlo simulations. We show that cation barriers have generally higher migration energies as compared to oxygen defects, which diffuse via correlated jumps. Moreover, there are distinct diffusion paths for anion and cation interstitials while structural vacancies within the bixbyite structure do not give rise to an enhanced diffusion.

## I. INTRODUCTION

Transparent conductive oxides (TCO) are one of the key materials in optoelectronic devices such as thin-film solar cells, organic light-emitting diodes, and flat panel displays. They are transparent within the visual range while their free electron concentration approaches values typical for metals.[1,2] Among the TCOs indium oxide ($In_2O_3$) and indium-tin oxide (ITO) play a particularly important role due to their excellent electronic properties in combination with a good processing characteristics and a high work function,[3,4] which makes them especially suitable for applications in devices containing organic functional layers.[5] The electronic structure of $In_2O_3$ is that of a wide gap semiconductor ($>2.6$ eV) (Refs. 6 and 7) providing the necessary transparency. The free-electron concentration, which may well exceed $10^{21}$ cm$^{-3}$, is usually obtained by tin doping[8,9] or by reduction in the undoped material. Free-electron concentrations of $10^{19}$ cm$^{-3}$ in the pure material indicate the presence of intrinsic point defects in high concentrations. Surprisingly, rather little is known about the mobility of point defects in $In_2O_3$. Relevant point defects have been identified from measurements of electronic conductivity as function of oxygen partial pressure[8–11] and from theoretical calculations within density-functional theory (DFT).[12,13] These results suggest the predominance of oxygen vacancies under reducing conditions and oxygen interstitials in oxidizing environments. Hitherto, migration paths and barriers of intrinsic defects, however, have not been investigated. To our knowledge there exist only few studies which have attempted to measure self-diffusion coefficients in $In_2O_3$.[14–16] In these studies, however, it was not possible to reliably extract the mobilities of the migrating defects, since the defect concentrations were either not measured along with the mobilities,[15,16] or the specimen contained impurities.[14] Generally, the determination of diffusion constants is complicated by the entanglement of formation energies with migration energies. While the migration energies are usually constant, the formation energies of the defects can change by several electron volts depending on Fermi energy and oxygen partial pressure.

In this study, we present a complete survey of diffusion processes of intrinsic point defects in $In_2O_3$. We systematically map out the total-energy surface by means of first-

principles calculations for possible migration paths and identify the relevant processes for each defect type in several charge states. In doing so, the role of the peculiar C-type rare-earth structure (bixbyite) and its influence on the defect mobilities is particularly addressed. Our results can be used in future studies to either interpret diffusion experiments or as a guide for annealing temperatures and defect equilibration temperatures.

The paper is organized as follows: we first introduce the underlying host crystal structure in Sec. III and discuss neighborhood relations and implications on diffusion and differences to the related fluorite structure. After describing the methodology, we present the results on oxygen and indium vacancies as well as the interstitials of both constituents in Secs. IV C and IV D. Finally, in Sec. V we discuss the accuracy of the results and conclude with a summary.

## II. METHODOLOGY

### Computational setup

DFT calculations were carried out using the Vienna *ab initio* simulation package (VASP).[17,18] The potentials due to the nuclei and the core electrons were represented by the projector augmented wave scheme by Blöchl.[19,20] The $4d$, $5s$, and $5p$ electrons of indium as well as the $2s$ and $2p$ electrons of oxygen were treated as part of the valence while the plane-wave cutoff energy was set to 500 eV. The generalized gradient approximation (GGA) in the parameterization by Perdew, Burke, and Ernzerhof[21] was selected to express the exchange-correlation potential. For Brillouin-zone integrations, a $3 \times 3 \times 3$ $k$-point mesh was employed. The GGA+$U$ method was adopted in the formulation by Dudarev *et al.*[22] with $\bar{U} - \bar{J} = 7$ eV, which we have tested previously within band structure as well as defect calculations.[13,23] This correction shifts the position of the $d$ states and also the band gap is widened while the lattice constant is reduced resulting in a better overall agreement of structural parameters with experimental data. For the calculation of the transition state energies we have applied the climbing image nudged-elastic-band[24,25] method, where initial and final positions are used as input data. Within this method the image closest to the saddle point will be driven onto the saddle
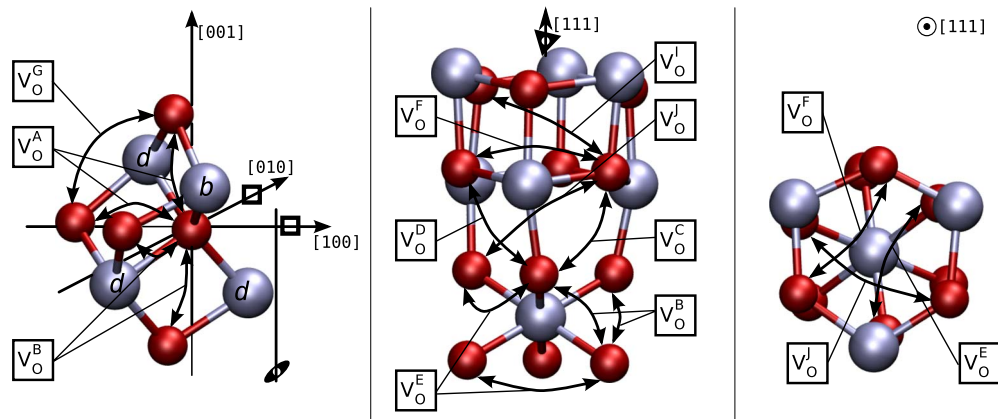
FIG. 1. (Color online) Nearest neighbors of the oxygen (left) and atomic arrangement surrounding the threefold axis (center/right). Rotation axis are included for orientation. Migration paths are indicated by their labels and the numeric values for the corresponding energy barriers can be found in Table I.

point during ionic relaxation. The energy barrier is defined as $\Delta E^M = E_{TS} - E_i$, the difference between the transition state energy and the ground state of the initial state.[26] The number of images (initial and final state not included) used for the determination of energy barriers ranged between 3 and 7, depending on the complexity of the diffusion path.

## III. CRYSTAL STRUCTURE

Indium oxide crystallizes predominantly in a cubic C-type rare-earth modification (bixbyite). The body-centered unit cell of $In_2O_3$ consists of 80 atoms (16 f.u.) with 48 oxygen and 32 indium atoms. There are 8 indium $b$ sites which differ from the remaining 24 $d$ sites by an $S_6$ site symmetry compared to $C_2$. In contrast, oxygen sites are all equivalent and occupy general lattice positions.

In terms of stacking sequence the indium and oxygen atoms are distributed on separate layers in {100} planes but on mixed {110} as well as {111} planes having the compound stoichiometry. Within the {100} planes, each of the four indium layers contains eight cations, while only every second layer contains the indium sites of higher symmetry. The four oxygen layers are equivalent but displaced with respect to each other by a glide mirror operation.

The bixbyite structure is also often described as a $2 \times 2 \times 2$ fluorite lattice. In order to obtain the bixbyite lattice from the latter, 12 anions need to be removed from the anion sublattice in a systematic way. Each {100} anion layer contains four of these vacant positions when compared with the fluorite lattice. These so-called structural vacancies are denoted by squares in subsequent illustrations, but should not be confused with thermal vacancies, which are formed on regular oxygen sites. The structural vacancy position is rather an interstitial site, and also the one which can accommodate interstitials of both constituents most easily, as it was shown previously.[12,13] In the fluorite lattice the anions have a tetrahedral cation and octahedral anion environment. Cations are surrounded by cubes of anion neighbors but have a face-centered cubic nearest cation neighborhood. Due to the structural vacancies, site symmetries are reduced when compared

with the fluorite lattice and there is a considerable structural distortion of the face-centered cubic arrangement of the cation positions.

In the bixbyite structure there are still four cation neighbors (one In-$b$ and three In-$d$) surrounding the anions in a strongly distorted tetrahedron arrangement. Further, the number of first anion neighbors is reduced to four.

Cations are now surrounded by only six anions and in two different conformations. The geometries can be obtained by removing anions from the body/face diagonal of the anion cubes (of the fluorite lattice) for the In-$b$/In-$d$ sites, respectively.

In the fluorite lattice atomic positions of different neighbor shells are structurally equivalent and therefore the corresponding energy barriers are identical. In the bixbyite structure, in contrast, the number of distinct migration barriers is significantly increased due to the reduced symmetry (see Figs. 1 and 2).

## IV. RESULTS AND DISCUSSION

### A. Migration mechanisms

Various defect types can occur in $In_2O_3$ depending on the environmental conditions. The oxygen vacancies are important for the pure material[10,27] and oxygen interstitials become important as soon as the material is $n$-type doped.[8] Defect studies have indicated the relevance of thermal indium vacancies[13,28] as well as oxygen dumbbell defects at higher oxygen pressures.[12,13] For completeness, we have also included the indium interstitials, although high formation energies were reported for this defect.[12,13] The complete set of data including the energy barriers, jump lengths and jump directions, as well as further details about the migration processes are given in Tables I–III. In order to obtain the full set of migration barriers within the unit cell, all symmetry elements of the space group 206 ($Ia\bar{3}$) can be applied to the representant processes given in the tables. Antisites as well as the effect of association of defects are presently not considered. It was shown earlier, that formation energies of antisites are rather high while association energies are negligi-
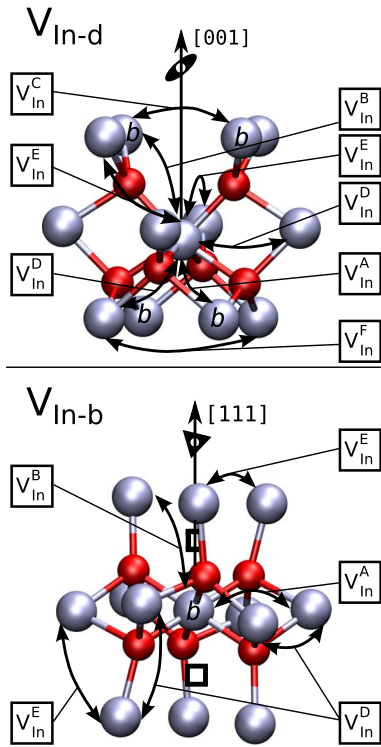
FIG. 2. (Color online) The nearest neighbors of the indium *d* (top) and indium *d* sites (bottom). Boxes indicate the locations of structural vacancies. Rotation axis are included for orientation. Migration paths are indicated by their labels and the numeric values for the corresponding energy barriers can be found in Table I

bly small.[13] Further, we want to stress that in highly *n*-type doped material defect association and interaction with extrinsic impurities is certainly important[8,9,29] but also not considered in the present study.

## B. Nomenclature

In the following the different migration processes are labeled by the defect symbol according to standard notation in conjunction with a capital letter superscript indicating a distinct microscopic diffusional jump. The superscript may additionally contain a number to indicate that there is more than one path leading to the same final state (e.g., interstitialcy processes). In the following images the processes are indicated by arrows connecting two sites.

Furthermore, it is generally possible for the defects to occupy different sublattices (e.g., indium vacancies) sites. For this reason defect processes are also separated with respect to the sublattice of the initial state (compare with Tables I–III)

There is a total of seven symmetrically distinct sites (sublattices) to be considered for diffusion which are labeled with italic lower case letters according to Wyckoff notation (compare with Sec. III). The general position (*e*) is relevant for oxygen vacancy diffusion while two sublattices (*b* and *d*) are involved for the cation vacancies. Both, oxygen and indium interstitials migrate on the structural vacancy site (*c*) whereas only for indium interstitials the high symmetry point

(*a*) is a stable site. Interstitials have furthermore the possibility to migrate via indirect interstitialcy mechanism, which involves regular lattice sites being the *e* site for oxygen interstitials and *b*/*d* sites for the indium interstitials. Finally, the oxygen dumbbell defect occupies the regular oxygen lattice position (*e*) with two different atoms. This can be thought of as two different general positions which are displaced from the original oxygen lattice site. In the following sections the lattice sites of the final states are also categorized in terms of neighbor shell relations and their respective crystallographic jump directions. For both, neighbor shells and directions the underlying fluorite lattice geometry is taken as reference in order to avoid large indices for directions and additional complications for neighbor relations.

## C. Vacancy mechanism

### 1. Oxygen vacancy

According to experiments, positively charged oxygen vacancies are the predominant defect type in $In_2O_3$. This is indicated by the characteristic oxygen partial pressure dependence ($\sigma \sim p_{O_2}^{-1/6}$) of the free-electron concentration.[10] Also, theoretical defect calculations predict the presence of oxygen vacancies.[12,13,30] The predominant charge state, however, is still under debate. In thermodynamic equilibrium, there will always be a fraction of neutral vacancies besides the ionized vacancies even for the case of a shallow donor defect. For this reason we have determined the barriers for the oxygen vacancies in all potentially occurring charge states ($q=0$, $+1,+2$). Figure 1 shows the direct neighborhood of the oxygen vacancies. All nearest-neighbor sites of the vacancy are located in $\langle 100 \rangle$ directions (Fig. 1 left). Migration processes to these target sites are only pairwise equivalent and denoted as processes $V_O^{\mathbf{A}}$ and $V_O^{\mathbf{B}}$, respectively. The two remaining $\langle 100 \rangle$ directions point toward structural vacancies (*c* sites). Since these directions are not blocked by any atom, we have also considered migration over the structural vacancy, for which the target site is located at large distance within the fourth-neighbor shell (process $V_O^{\mathbf{J}}$ in Fig. 1 center/right).

The second-neighbor shell comprises nine sites located in $\langle 110 \rangle$ directions from which 6 are geometrically accessible (not blocked by cations). They are connected by migration processes labeled $V_O^{\mathbf{C}}$-$V_O^{\mathbf{G}}$. The remaining three $\langle 110 \rangle$ directions again lead to vacant positions. Processes $V_O^{\mathbf{D}}$, $V_O^{\mathbf{E}}$, $V_O^{\mathbf{F}}$ are twofold and represent mechanisms which lead to circulating motions with no net displacement, if considered separately (the same is true for processes $V_O^{\mathbf{A}}$ and $V_O^{\mathbf{B}}$). Transitions $V_O^{\mathbf{C}}$, $V_O^{\mathbf{G}}$ on the other hand are only onefold and their saddle points are aligned on the twofold rotation axis. Transition $V_O^{\mathbf{C}}$, appears to be of special interest, since its saddle-point configuration has two structural vacancies in its proximity, and therefore exhibits the lowest oxygen vacancy barrier in any charge state (e.g., $\Delta E^M[+2]=0.71$ eV). Note that this process represents a migration to the second-neighbor shell in $\langle 011 \rangle$ direction (Fig. 1 center).

The six third neighbors are located in $\langle 111 \rangle$ directions among which three processes are completely blocked by cations and therefore are not considered as possible migration processes. Additionally, another two sites are vacant within

TABLE I. Collection of migration barriers for bixbyite indium oxide including oxygen and indium vacancy mechanism. The first column contains the defect type and its location within the unit cell. The label used in images is given in column three followed by the corresponding jump distance $\lambda$ and the migration energies $\Delta E^M$ in the relevant charge states. Column five gives the multiplicity of the corresponding process (number of times the process is available by symmetry from one site). The last column contains one representant of the corresponding jump vector.

| Defect | Process | $\lambda$ (Å) | $\Delta E^M[q]$ (eV) | | | | | | | Multiplicity | Direction $x,y,z$ |
|---|---|---|---|---|---|---|---|---|---|---|---|
| | | | $-3$ | $-2$ | $-1$ | $0$ | $+1$ | $+2$ | $+3$ | | |
| $V_O$ | $V_O^A$ | 2.79 | | | | 1.73 | 1.09 | 0.99 | | 2 | $(0.08, 0.44, -2.75)$ |
| $(x=0.390)$ | $V_O^B$ | 2.81 | | | | 2.00 | 1.37 | 1.28 | | 2 | $(0.44, 0.36, 2.75)$ |
| $(y=0.154)$ | $V_O^C$ | 2.94 | | | | 1.53 | 0.77 | 0.71 | | 1 | $(-2.22, -1.93, 0.00)$ |
| $(z=0.382)$ | $V_O^D$ | 3.29 | | | | 2.08 | 1.53 | 1.50 | | 2 | $(0.44, -2.30, -2.30)$ |
| | $V_O^E$ | 3.31 | | | | 2.07 | 1.40 | 1.35 | | 2 | $(0.08, -2.38, 2.30)$ |
| | $V_O^F$ | 3.54 | | | | 2.09 | 1.76 | 1.80 | | 2 | $(-2.30, 2.67, 0.36)$ |
| | $V_O^G$ | 3.71 | | | | 3.93 | | 3.82 | | 1 | $(2.83, 0.00, -2.39)$ |
| | $V_O^H$ | 4.47 | | | | | | 5.72 | | 2 | $(-2.67, -2.30, 2.75)$ |
| | $V_O^I$ | 4.51 | | | | | | 4.72 | | 1 | $(-2.22, 3.11, -2.39)$ |
| | $V_O^J$ | 4.62 | | | | 2.65 | | 2.55 | | 2 | $(0.08, -4.61, 0.36)$ |
| $V_{In-b}$ | $V_{In-b}^A$ | 3.34 | 2.46 | 2.31 | | | | | | 6 | $(0.00, -2.19, 2.52)$ |
| $(\frac{1}{4}, \frac{1}{4}, \frac{1}{4})$ | $V_{In-b}^B$ | 3.82 | 6.85 | | | | | | | 6 | $(0.00, -2.86, -2.52)$ |
| | $V_{In-b}^C$ | 5.05 | 4.97 | | | | | | | 6 | $(0.00, 0.00, -5.05)$ |
| $V_{In-d}$ | $V_{In-d}^A$ | 3.34 | 2.27 | 2.29 | | | | | | 2 | $(2.19, -2.52, 0.00)$ |
| $(x=0.467)$ | $V_{In-d}^B$ | 3.82 | 6.65 | | | | | | | 2 | $(-2.86, -2.52, 0.00)$ |
| $(y=0.0)$ | $V_{In-d}^D$ | 3.36 | 2.42 | 2.30 | | | | | | 4 | $(-0.33, -2.52, 2.19)$ |
| $(z=\frac{1}{4})$ | $V_{In-d}^E$ | 3.83 | 2.08 | 2.11 | | | | | | 4 | $(-0.33, -2.52, -2.86)$ |
| | $V_{In-d}^F$ | 5.05 | 4.54 | | | | | | | 2 | $(-5.05, 0.00, 0.00)$ |
| | $V_{In-d}^G$ | 5.10 | 4.54 | | | | | | | 2 | $(-0.67, 0.00, -5.05)$ |
| | $V_{In-d}^H$ | 5.10 | 4.98 | | | | | | | 2 | $(0.00, -5.05, 0.00)$ |

this neighbor shell. Only $V_O^H$ and $V_O^I$ remain as possible migration processes, where $V_O^I$ corresponds to a migration via an $a$-interstitial site. The corresponding migration energies are, however, rather high ($\Delta E^M[+2] \approx 5$ eV). In total, we have calculated the barriers for ten symmetrically distinct transitions (see Table I), giving rise to 17 transitions in total.

A remarkable feature of the oxygen vacancy diffusion is that each specific transition occurs with a maximum multiplicity of two. Apparently, not every site on the oxygen sublattice can be reached using only one specific type of process. At least two active mechanisms are necessary in order to allow for larger displacements within the oxygen sublattice. Our findings imply a mixed $V_O^C$, $V_O^A$ motion at low temperatures and some additional contribution of $V_O^B$, $V_O^E$, and $V_O^D$ at elevated temperatures. Transitions via long jumps through the structural vacancies ($V_O^J$) have a surprisingly low-energy barrier ($\Delta E^M[+2] = 2.55$ eV) when compared with other processes of similar jump distance ($V_O^H$ and $V_O^I$). This energy barrier is, however, still too high in order to significantly contribute to oxygen diffusion at relevant temperatures.

### 2. Indium vacancy

For In$_2$O$_3$, cation vacancy diffusion is assumed to be negligibly low because of the small estimated concentration of

vacancies. [8,14] This assumption is, however, not necessarily justified at higher temperatures[28] and high $n$-type doping levels. Moreover, indium vacancies provide a possible migration path for the technologically important cation dopants (tin) for which a considerably mobility has already been reported in the literature.[4]

The formation energies of vacancies of the two distinct indium lattice sites $V_{In-b}$ and $V_{In-d}$ differ by less than $\Delta E \approx 0.2$ eV for all possible charge states. [12,13] Since there are two different sites with similar stability, both sublattices may contribute to material transport via indium vacancies. Therefore, it is useful to discuss individual jump processes which connect only $b$ or $d$ sites and mixed processes connecting $b$ with $d$ sites, separately. The predominant charge state over a wide range of Fermi energies was shown to be $q=-3$ on which we also focus here.[12,13] We have, however, also calculated the barriers for $q=-2$ in order to study the charge state dependence of migration.

There is only one process of the first type ($b$ to $b$), which can be considered as a possible migration path. The target site is located toward $\langle 100 \rangle$ directions and separated by a rather large distance of 5.05 Å. There is no blocking along the migration path but due to the large migration distance the energy barrier is high as $\approx 5$ eV (process $V_{In}^C$) and therefore not activated at relevant temperatures.

TABLE II. Collection of migration barriers for oxygen and indium interstitials. The first column contains the defect type and its location within the unit cell. The label used in images is given in column three followed by the corresponding jump distance $\lambda$ and the migration energies $\Delta E^M$ in the relevant charge states. Column five gives the multiplicity of the corresponding process (number of times the process is available by symmetry from one site). Column six is one representant of the corresponding jump vector. The last column contains the angle and jump distance of the lattice atom in the case of intersticialcy mechanism.

| Defect | Process | $\lambda$ (Å) | $\Delta E^M[q]$ (eV) | | | | | | | Multiplicity | Direction $x,y,z$ | Angle→distance (Å) |
| | | | $-3$ | $-2$ | $-1$ | $0$ | $+1$ | $+2$ | $+3$ | | | |
|---|---|---|---|---|---|---|---|---|---|---|---|---|
| $O_i$ | $O_i^A$ | 3.62 | | 1.22 | 0.52 | | | | | 1 | (2.09, 2.09, 2.09) | |
| ($x=0.397$) | $O_i^B$ | 3.63 | | 2.42 | | | | | | 3 | (2.09, −2.96, 0.00) | |
| ($y=0.397$) | $O_i^{B1}$ | 2.22 | | 1.38 | 0.77 | | | | | 3 | (−0.15, 2.15, −0.51) | 101.6→2.46 |
| ($z=0.397$) | $O_i^{B2}$ | 2.45 | | 1.38 | 0.77 | | | | | 3 | (−0.06, −2.45, −0.15) | 101.6→2.22 |
| | $O_i^{C1}$ | 2.45 | | 2.98 | | | | | | 3 | (−0.06, −2.45, −0.15) | 133.1→3.90 |
| | $O_i^{C2}$ | 3.90 | | 2.98 | | | | | | 3 | (−0.15, −2.90, 2.60) | 133.1→2.46 |
| | $O_i^{D1}$ | 2.45 | | 1.47 | | | | | | 3 | (−0.06, −2.45, −0.15) | 135.7→3.44 |
| | $O_i^{D2}$ | 3.43 | | 1.47 | | | | | | 3 | (−0.06, 2.60, 2.24) | 135.7→2.46 |
| | $O_i^{E1}$ | 2.45 | | 4.16 | | | | | | 3 | (−0.06, −2.45, −0.15) | 100.7→4.08 |
| | $O_i^{E2}$ | 4.07 | | 4.16 | | | | | | 3 | (−0.51, −2.81, −2.90) | 100.7→2.46 |
| $In_{i-c}$ | $In_{i-c}^{A1}$ | 2.23 | | | | | | 1.36 | 1.62 | 1 | (1.29, 1.29, 1.29) | |
| ($x=0.372$) | $In_{i-c}^{B}$ | 3.57 | | | | | | 2.16 | 2.75 | 3 | (0.00, 2.58, −2.47) | |
| ($y=0.372$) | $In_{i-c}^{B1}$ | 2.42 | | | | | | 1.64 | 1.69 | 3 | (−1.23, 1.62, 1.29) | 95.35→2.42 |
| ($z=0.372$) | $In_{i-c}^{C1}$ | 2.14 | | | | | | 0.29 | 0.42 | 1 | (−1.23, −1.23, −1.23) | 180.00→2.15 |
| $In_{i-a}$ | $In_{i-a}^{A1}$ | 2.23 | | | | | | 0.67 | 0.99 | 2 | (−1.29, −1.29, −1.29) | |

Sites of $d$ type can be found in closer proximity, i.e., the nearest neighbors for In-$b$ consist only of In-$d$ which are distributed in a distorted face-centered cubic arrangement around In-$b$ (Fig. 2). Two symmetrically inequivalent migration processes can be identified within this nearest-neighbor shell of In-$b$. Taking a (111) plane as the reference as it is denoted in Fig. 2 processes $V_{In}^A$ are in-plane motions whereas $V_{In}^B$ has out of plane components which lead to significantly different migration energies. While the barrier for the in-plane motion is 2.46 eV the out-of-plane migration is sup-

TABLE III. Collection of migration barriers for oxygen dumbbell defect. The first column contains the defect type and its location within the unit cell. The labels of the processes are given in column three followed by the corresponding jump distance $\lambda$ and the migration energies $\Delta E^M$ in the relevant charge states. Column five gives the multiplicity of the corresponding process (number of times the process is available by symmetry from one site). Column six is one representant of the corresponding jump vector. The last column contains the sites which are connected by the respective process.

| Defect | Process | $\lambda$ (Å) | $\Delta E^M[q]$ (eV) | | | | | | | Multiplicity | Direction $x,y,z$ | Sites |
| | | | $-3$ | $-2$ | $-1$ | $0$ | $+1$ | $+2$ | $+3$ | | | |
|---|---|---|---|---|---|---|---|---|---|---|---|---|
| $O_{i,db-1}$ | $O_{db-1}^X$ | 1.52 | | | | 0.87 | | | | 1 | (0.76, −0.14, 1.30) | $O_{i,db-1} \rightarrow O_{i,db-2}$ |
| ($x=0.390$) | $O_{db-1}^Y$ | | | | | 2.46 | | | | 2 | | $O_{i,db-1} \rightarrow O_{i-a}$ |
| ($y=0.154$) | $O_{db-1}^Z$ | | | | | 1.43 | | | | 1 | | $O_{i,db-1} \rightarrow O_{i-c}$ |
| ($z=0.382$) | $O_{db-1}^B$ | 1.74 | | | | 1.68 | | | | 2 | (−0.13, 0.21, −1.71) | $O_{i,db-1} \rightarrow O_{i,db-1}$ |
| | $O_{db-1}^C$ | 3.22 | | | | 2.06 | | | | 1 | (2.22, 1.93, 1.30) | $O_{i,db-1} \rightarrow O_{i,db-2}$ |
| | $O_{db-1}^D$ | 2.82 | | | | 1.35 | | | | 1 | (2.03, −0.90, −1.72) | $O_{i,db-1} \rightarrow O_{i,db-2}$ |
| | $O_{i,db-1}^E$ | 2.52 | | | | 1.00 | | | | 2 | (−0.35, 1.93, −1.58) | $O_{i,db-1} \rightarrow O_{i,db-1}$ |
| $O_{i,db-2}$ | $O_{db-2}^X$ | 1.52 | | | | 0.87 | | | | 1 | (−0.76, 0.14, −1.30) | $O_{i,db-2} \rightarrow O_{i,db-1}$ |
| ($x=0.390$) | $O_{db-2}^A$ | 2.18 | | | | 1.40 | | | | 1 | (0.18, −0.76, 2.03) | $O_{i,db-2} \rightarrow O_{i,db-2}$ |
| ($y=0.154$) | $O_{db-2}^C$ | 3.22 | | | | 2.06 | | | | 1 | (2.22, 1.93, −1.30) | $O_{i,db-2} \rightarrow O_{i,db-1}$ |
| ($z=0.382$) | $O_{db-2}^D$ | 2.82 | | | | 1.35 | | | | 1 | (−0.90, 1.72, 2.03) | $O_{i,db-2} \rightarrow O_{i,db-1}$ |
| | $O_{db-2}^F$ | 2.73 | | | | 1.19 | | | | 2 | (1.27, −2.21, −0.94) | $O_{i,db-2} \rightarrow O_{i,db-2}$ |

pressed ($>6$ eV) due to close encounters with anions leaving process $V_{In}^A$ the only relevant exchange mechanism between $b$ and $d$ sites.

A greater diversity of transitions is found originating from $d$ sites due to their lower symmetry. For the nearest-neighbor shell four distinct processes can be identified ($V_{In}^A$, $V_{In}^B$, $V_{In}^D$, and $V_{In}^E$) instead of two (for In-$b$). Transitions $V_{In}^A$ and $V_{In}^B$ are both twofold and connect back to the In-$b$ sites. The energy barriers differ by the difference of defect formation energy between the indium vacancies on the two sites. The remaining processes $V_{In}^D$ and $V_{In}^E$ are both fourfold and lead to continued migration on the In-$d$ sublattice with comparably low barriers of 2.42 eV and 2.08 eV, respectively. Processes at larger distances involve energy barriers higher than 4 eV and do not contribute to diffusion (processes $V_{In}^F$, $V_{In}^G$, and $V_{In}^H$).

In total, the low-energy paths involve the process $V_{In}^A$ which connects the two sublattices $b$ and $d$ as well as transitions $V_{In}^E$ connecting only $d$ sites. The $b$ site is by 0.2 eV more favorable when compared with $d$ sites. This result suggests that indium vacancies have a longer residence time on $b$ sites. However, once a vacancy moves, it will be located on a symmetrically different site, and migration takes mainly place on the other sublattice. The corresponding migration process on the In-$d$ sublattice offers a complete set of transitions to reach any site within the lattice. The diffusion is mediated via $d$ sites although $b$ sites are more stable.

### D. Interstitial mechanism

#### 1. Oxygen interstitial

In the bixbyite lattice the 16$c$ positions offer a relatively large volume for the accommodation of interstitial defects. Indeed, the oxygen interstitials are of major technological interest for the $n$-type doped material.[8,29] In the charge state $q=-2$ they are conjectured to be the main source of electron compensation in ITO.[8] However, the unit cell comprises 80 atoms and 16 interstitial sites are therefore well separated from each other. The neighbor relations of the interstitial positions are depicted in Fig. 3 and the corresponding energy barriers can be found in Table II. The interstitial sites are aligned chainlike in $\langle 111 \rangle$ directions and alternatingly separated by interstitial $a$ positions and In-$b$ cations.

The closest neighbor is reached just along the $\langle 111 \rangle$ direction. This is a onefold process since the opposite direction ($[\bar{1}\bar{1}\bar{1}]$) is blocked by an In-$b$ cation. This process ($O_i^A$) involves traversing an interstitial $a$ site, which for oxygen interstitials in charge state $q=-2$ is a saddle-point configuration.

The three second neighbors are located toward $\langle 110 \rangle$ directions and perpendicular to process $O_i^A$. The jump distance of this process $O_i^B$ is rather large (3.63 Å) and additionally cations partly obstruct the diffusion path (Fig. 3). Therefore, the corresponding interstitialcy processes involving the regular lattice sites (processes $O_i^{B1}$ and $O_i^{B2}$ in Fig. 3) need to be considered and compared with the direct process. The interstitialcy processes may occur via two different lattice oxygen sites depicted in Fig. 3. By symmetry, however, both processes $O_i^{B1}$ and $O_i^{B2}$ are equivalent in energy and offer an
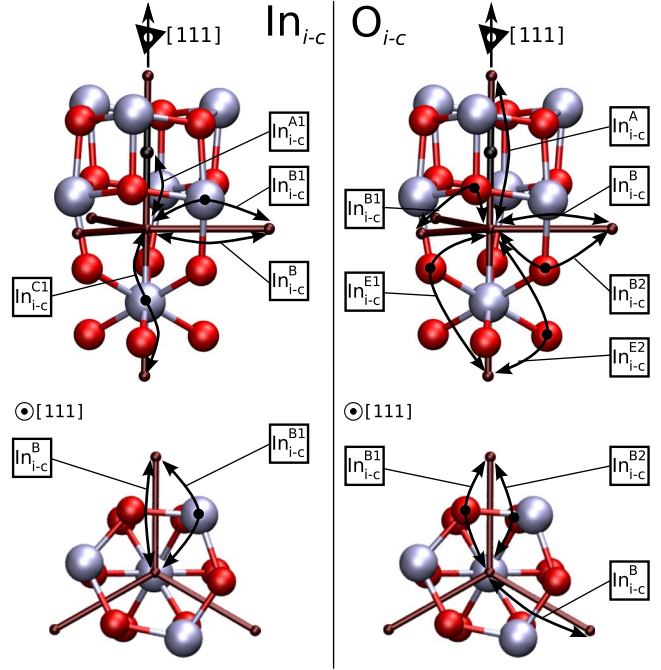


FIG. 3. (Color online) Nearest neighborhood of the interstitial positions for In$_{i-c}$ (left) and O$_{i-c}$ (right). The nearest interstitial positions are connected. The additionally stable stationary point ($a$ site) for indium interstitials is denoted by a black ball. Rotation axis are included for orientation. Migration paths are indicated by their labels and the numeric values for the corresponding energy barriers can be found in Table II.

effective multiplicity of six compared to three for the direct process. The interstitialcy processes have significantly lower migration energies when compared with the direct ones (1.38 vs 2.42 eV). Furthermore, interstitialcy jumps to even larger distances can be constructed (process $O_i^{D1}/O_i^{D2}$) with only slightly higher-energy barriers (1.48 eV). In this case, no direct transition is geometrically realizable. Similarly, the path $O_i^E$ in $[\bar{1}\bar{1}\bar{1}]$ direction is blocked by an indium atom (Fig. 3) but two interstitialcy processes ($O_i^{E1}$ and $O_i^{E2}$) can be constructed, which are again symmetrically equivalent. These events have high migration energies and are not likely to play a role.

The lowest migration barrier for oxygen interstitial diffusion is process $O_i^A$ (1.22 eV). Similar like in the case of oxygen vacancies this single process is not sufficient to provide a complete diffusion path. In order to reach any interstitial site of the lattice, interstitialcy jumps via $O_i^{B1}/O_i^{B2}$ are needed. The rate determining transitions are therefore $O_i^{B1}$ and $O_i^{B2}$. In between these events $O_i^A$ will be active, however, not lead to any net displacement but only to an exchange of the interstitial between two $c$ sites in nearest neighborhood.

#### 2. Indium interstitial

For indium interstitial diffusion the same sublattice as for the oxygen interstitials is used. The minimum energy position of the interstitial is located closer to the In-$b$ atom when compared with the oxygen interstitials (compare values of
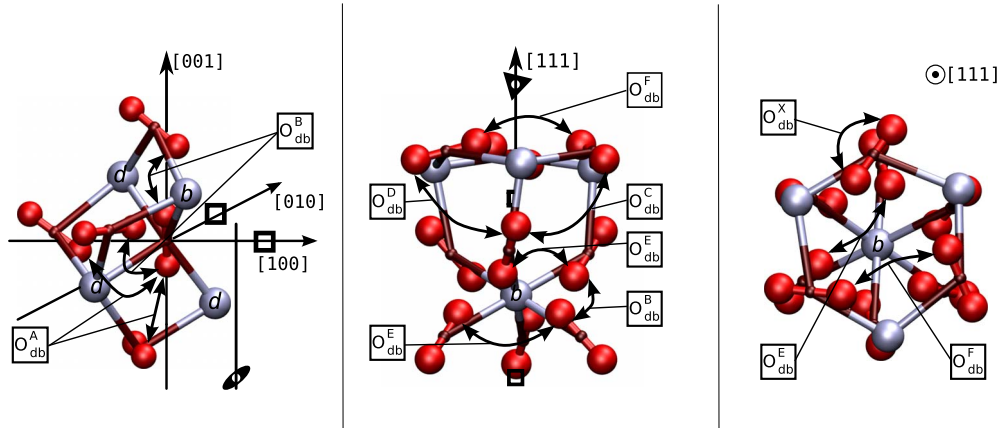
FIG. 4. (Color online) First neighbors of the oxygen site when occupied by a dumbbell defect (left). View along an ⟨111⟩ axis from the side (center) and from the top (right). The most important jump processes are labeled within the images.

first column in Table II) Additionally, the interstitial *a* site is a stable minimum with an increased formation energy of 0.6 eV for indium interstitials, whereas it is simply a saddle-point configuration for oxygen interstitials.

There is one unique process ($\mathrm{In}_i^{\mathbf{A1}}$) connecting *c* with *a* positions. The decay back to a regular interstitial site can occur to either side along ⟨111⟩ (Fig. 3 left). In contrast to the case of oxygen interstitials, the $[\bar{1}\bar{1}\bar{1}]$ direction is available for migration via an interstitialcy mechanism ($\mathrm{In}_i^{\mathbf{C1}}$). Energetically, the latter process also constitutes the lowest-energy transition for indium interstitials with a remarkably low barrier of 0.42 eV in the charge state +3. The opposite direction toward the *a* site is considerably higher (1.62 eV) but still lower in transition energy than processes leading away from the ⟨111⟩ axis (1.69 eV).[31] Interstitialcy processes leading away from the ⟨111⟩ axis ($\mathrm{In}_i^{\mathbf{B1}}$) are again favored over direct mechanisms ($\mathrm{In}_i^{\mathbf{B}}$). Compared to oxygen interstitials the multiplicity of this mechanism is only three due to the smaller number of neighboring indium cations.

For indium interstitials comparable energy barriers were found as for oxygen interstitial diffusion ($\approx$1.3–1.5 eV), however, the overall mechanism is very different. In the case of oxygen, transitions leading away from ⟨111⟩ axis ultimately determine the activation for diffusion although processes along ⟨111⟩ are always faster. For indium interstitials, the *b*-lattice indium does not play a constraining role within ⟨111⟩ direction and the data suggests another mode of migration. Here, the ⟨111⟩ axes can serve as quasi-one-dimensional diffusion channels with a sequence of processes …$\mathrm{In}_{i-c}^{\mathbf{C1}} \rightarrow \mathrm{In}_{i-c}^{\mathbf{A1}} \rightarrow \mathrm{In}_{i-a}^{\mathbf{A1}}$…. Depending on temperature the interstitials can change to other ⟨111⟩ channels via $\mathrm{In}_{i-c}^{\mathbf{B1}}$.

### 3. Oxygen dumbbell interstitial

The oxygen dumbbell interstitial is a covalently bonded oxygen dimer defect located on a regular lattice site. This defect can be found in several orientations.[13] The most stable form of the dumbbell is the neutral charge state. We have shown in a previous study[13] that for the neutral charge state the regular oxygen interstitial *c* sites denote only very shallow or no minima on the total-energy surface and can there-

fore be considered as transition states for the oxygen dumbbell rather than stationary intermediate configurations. Further, only the dumbbell configuration in its most stable configuration is considered for migration in the present study.

Since the motion of the dumbbell is exclusively restricted to the regular oxygen sublattice similar considerations apply for possible migrations mechanisms as for the oxygen vacancies. The difference, however, is that there are now two particles attempting a jump. As a consequence, each process of the oxygen vacancy diffusion generally results in four distinct processes. For the same reason also Table III is split into two parts for $\mathrm{O}_{i,\mathrm{db}-1}$ and $\mathrm{O}_{i,\mathrm{db}-2}$, respectively. The $\mathrm{O}_{i,\mathrm{db}-1}$ is the oxygen, which has In-*b* as nearest cation neighbor (Fig. 4 left).

In Fig. 4 the neighboring oxygen dumbbell orientations of the first- and second-neighbor shells of the oxygen sites are shown. For each oxygen site two atoms are depicted with their varying relative dimer axis orientations. Due to the vast number of possible processes we have only considered transitions for which the analogous oxygen vacancy mechanism barriers did not exceed 2.5 eV. Moreover, the number of processes can further be decreased by symmetry and geometrical considerations. For example, we have mainly considered processes where the ground-state configurations of the dimer on initial and target sites assume an approximately head to head configuration. Beside site to site jumps, the oxygen dumbbell can perform an on-site rotation i.e., instantaneous exchange of $\mathrm{O}_{i,\mathrm{db}-1}$ with $\mathrm{O}_{i,\mathrm{db}-2}$ atoms with an energy barrier of 0.87 eV.

The lowest corresponding migration energies for the dumbbell migration do neither comprise the first-neighbor shell ($\mathrm{O}_{\mathrm{db}-2}^{\mathbf{A}}$ and $\mathrm{O}_{\mathrm{db}-1}^{\mathbf{B}}$) nor process $\mathrm{O}_{\mathrm{db}-1}^{\mathbf{C}}$, for which the lowest migration energies were found in the case of the oxygen vacancies. These processes have migration energies of 1.40 eV, 1.68 eV, and 2.06 eV for $\mathrm{O}_{\mathrm{db}-2}^{\mathbf{A}}$, $\mathrm{O}_{\mathrm{db}-1}^{\mathbf{B}}$, and $\mathrm{O}_{\mathrm{db}-1}^{\mathbf{C}}$, respectively. In the case of the oxygen dumbbell, the lowest migration energies are found among jumps which direct the defect around the threefold rotation axis ($\mathrm{O}_{i,\mathrm{db}-1}^{\mathbf{E}}$ and $\mathrm{O}_{\mathrm{db}-2}^{\mathbf{F}}$) and are part of the second-neighbor shell of the oxygen sublattice. This is plausible, since the dumbbell consists of a surplus atom and the structural vacancies are all aligned on threefold

TABLE IV. Effective migration energies $\Delta E_{eff}^M$ and effective diffusion length $\lambda$ for all defects in two different temperature regimes. Additionally, the lowest-energy path with its corresponding jump distance is given. The effective migration energy is generally higher when compared with the lowest migration energies. The last column contains the annealing temperature which indicates the temperature range in which the defect becomes significantly mobile.

| Defect | $q$ | $\Delta E_{eff}^M$ (eV) | $\lambda_{eff}$ (Å) | $\Delta E_{eff}^M$ (eV) | $\lambda_{eff}$ (Å) | $\Delta E_{\min}^M$ (eV) | $\lambda_{\min}$ (Å) | $T_{an}$ (°K) |
|---|---|---|---|---|---|---|---|---|
| | | 1700–1500 K | | 700–900 K | | | | |
| $V_O$ | 0 | 1.83 | 3.49 | 1.77 | 2.44 | 1.53 | 2.94 | 640 |
| | +1 | 1.20 | 3.58 | 1.13 | 2.39 | 0.77 | 2.94 | 410 |
| | +2 | 1.10 | 3.32 | 1.02 | 2.26 | 0.71 | 2.94 | 370 |
| $V_{In}$ | −3 | 2.26 | 4.09 | 2.27 | 4.24 | 2.21 | 3.83 | 820 |
| | −2 | 2.21 | 4.13 | 2.17 | 3.35 | 2.11 | 3.83 | 800 |
| $O_i$ | −2 | 1.41 | 6.36 | 1.40 | 5.96 | 1.22 | 3.62 | 480 |
| | −1 | 0.74 | 3.94 | 0.77 | 4.62 | 0.52 | 3.62 | 270 |
| $O_{i,db}$ | 0 | 1.19 | 2.52 | 1.20 | 2.65 | 1.00 | 2.52 | 430 |
| $In_i$ | +3 | 1.67 | 7.27 | 1.66 | 7.08 | 0.42 | 2.14 | 580 |
| | +2 | 1.44 | 5.99 | 1.39 | 4.41 | 0.29 | 2.14 | 500 |

axis. Figure 4 shows the relative orientations of dimers in an arrangement close to the threefold rotation axis. The exchange process for these transitions is probably facilitated by the presence of the structural vacancy which is not the case for the nearest-neighbor processes ($O_{db-2}^A$ and $O_{db-2}^B$). These two low-energy processes, however, do not suffice to provide migration to all oxygen lattice sites. For a net displacement at least three different migration mechanisms need to be active. Our results suggest that beside the low-energy processes $O_{i,db-1}^E$ (1.01 eV) and $O_{db-2}^F$ (1.20 eV) process $O_{db-1}^D$ (1.35 eV) needs to be additionally active (see Fig. 4).

### E. Effective values and annealing temperatures

In order to use our data for obtaining macroscopic diffusion parameters, the set of migration barriers for each defect in a certain charge state needs to be averaged in an appropriate way. From the findings in Secs. IV C and IV D it is clear that for all defects (except $V_{In}$) the lowest-energy processes do not build a closed diffusion path. As it was also shown for several defects more than one sublattice is necessarily used during migration in $In_2O_3$. It therefore cannot be expected that the effective migration energy (which can be experimentally measured) will only be dominated by the migration processes with the lowest energy. In order to appropriately evaluate the contribution of each barrier to the effective migration energy $\Delta E_M^{eff}$ we have adopted a kinetic Monte Carlo (KMC) algorithm[32] in order to evaluate the mean-square displacement for each defect in its different charge states. We have performed a random walk on the respective sublattices and included all calculated barriers. The mean-square displacement was averaged for each temperature until $\Delta E_M^{eff}$ and $\lambda_M^{eff}$, the effective migration barrier and jump length, were converged to a relative error better than $10^{-2}$. The resulting values are listed in Table IV and given for two different temperature ranges. We find that, generally, both the effec-

tive jump length and the effective exponential factor become slightly temperature-dependent parameters. For an estimate of the absolute jump frequencies, from the transition probabilities, effective attempt frequencies are additionally needed. The values can be approximated on the basis of phonon calculations, which we have presented previously[28] and which also agree with IR-absorption data.[2] For diffusion of oxygen species ($V_O$ and $O_i$) and indium species ($V_{In}$ and $In_i$) we have used 15 THz and 5 THz, respectively. They are obtained by averaging over the corresponding partial phonon densities of state and mainly account for the differing masses of the two constituents. The total effective jump frequency was also converted into an "annealing temperature," which indicates the temperatures at which a particular defect becomes significantly mobile, i.e., when a specific defect type can equilibrate its population in the material in some reasonable time. As a definition we use the temperature at which the diffusion constant for the specific defect reaches a value of $10^{-12}$ cm$^2$ s$^{-1}$ and the corresponding temperature for each defect is listed in Table IV.[33] The value is largely dominated by the exponential term and does not severely suffer by the approximation of the attempt frequencies. Note that $\Delta E_M^{eff}$ generally differs from the lowest migration barrier for any defect type which is also given in the same table.

#### 1. Mobile defects

From Table IV it can be readily seen that oxygen vacancies in their presumably most stable charge state +2 become significantly mobile already at slightly elevated temperatures of about 400 K. In contrast, the indium vacancies do not get mobile before reaching temperatures of at least 820 K, which is not relevant in most technical applications but for diffusion measurements.[14,15] The difference is much less pronounced for the interstitials in the predominant charge states +3 and −2 for indium interstitials and oxygen interstitials,

respectively. They become mobile in a temperature range around 500–600 K, which are relatively high values for interstitial diffusion. The dumbbells on the other hand have an annealing temperature comparable with that of the oxygen vacancies in charge state +2. To our knowledge, no dedicated annealing experiments (after irradiation) have been performed on $In_2O_3$ yet, so that comparison can only be done indirectly. Wirtz and Takiar[14] have derived the chemical diffusion constant from relaxation measurements and extracted 1.5 eV and 1.4 eV for the migration energies of $O''_{i-c}$ and $V_O^{\cdot\cdot}$, respectively. Considering the statistical accuracy of their measurement and the impure sample, the agreement with our calculations (1.4 and 1.10 eV) is good. It is especially noteworthy that the oxygen interstitial migration is found to have a larger effective migration energy in both, theory and experiment. Furthermore, studies on the electrical conductivity[10,11,27] show annealing effects (irreversible change of conductivities) at temperatures of $\approx 400$ K which can be related to the activation of oxygen vacancy migration in charge state +2.

### 2. Role of the structural vacancy

The presence of the vacant sites in the bixbyite structure influences diffusion in two different ways. First, the point symmetry of all sublattices is lowered and generally a greater variety of different barrier heights can be identified. Due to the increased free volume, jumps toward these interstitial sites are usually lowered. However, for the oxygen and interstitial sublattices the lowest barriers do not offer a complete migration path via which a net diffusion can occur for a defect as we have shown. The lowest-energy barriers therefore do not contribute to the migration energy in these cases but to the prefactor for diffusion by connecting two lattice sites and increasing the multiplicity of the remaining mechanisms. This also means that the available free volume in $In_2O_3$ when compared with other $CaF_2$ derived structures does not result in a necessarily higher diffusion in the material as far as the barriers are concerned. Nevertheless, the structural vacancies enable the structure to accommodate large numbers of interstitial defects, which contribute to the total diffusion coefficient via the defect concentrations. The main effect of the structural vacancies is the break in symmetry and the resulting break of degeneracy in the migration processes.

### 3. Charge state dependence

As it is shown in Fig. 5 for all defects a charge state dependence of migration energies is found. The effect is mostly homogeneous for all processes (oxygen interstitials are an exception) of one particular defect type. While the migration energies tend to be low in the case of lower charge states, the opposite is true for the oxygen vacancies. Generally, the migration energies for $V_O$ are increased by $\approx 0.7$ eV when compared with the ionized vacancies ($q = +1/+2$). The charge state dependence is most important for the case of oxygen interstitials and to a lesser extent for the indium vacancies. Since the $q = -2$ and $q = -3$ charge state are most stable for these defects the charge state dependence has also
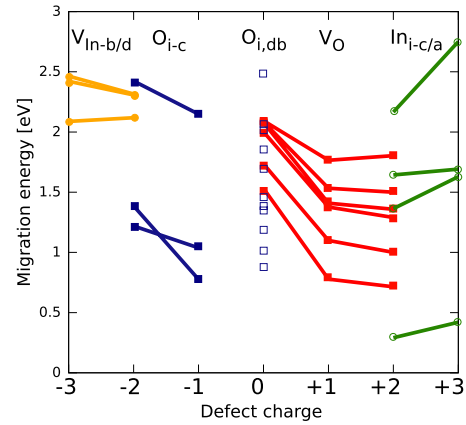


FIG. 5. (Color online) The charge state dependence for several barriers and all defect types. The order of barrier heights is mostly kept with changing charge state.

a further implication. For these charge states the electrons occupy acceptor states, which, in principle, can be removed under illumination. Based on our results the deionized defects (lower charge state) have a higher mobility which could lead to a light induced enhancement of diffusion. The absorption energies should lie little below the band-gap width since the acceptor defect states are found close to the valence-band maximum and no significant charge-state-dependent relaxation occurs for these defects. Therefore, we suggest that an enhanced bulk equilibration due to illumination could be possible. In experiments such an effect has already been observed for $In_2O_3$ [34] and is now well explained by our findings. We suggest the oxygen interstitials to be responsible for enhanced oxygen diffusion under UV illumination. Furthermore, we point out that this effect could also lead to aging effects in optoelectronic devices especially with organic materials and at short wavelengths of light.

## V. ACCURACY

The numerical accuracy of the total-energy calculations does only marginally affect the total error of the defect calculations, when compared with other potential sources of errors. Energy differences are taken of very similar configurations with the same number of atoms so that numerical inaccuracies should greatly cancel.

We assume the errors of the calculation to arise either from finite cell size effects or due to problems connected with the exchange-correlation functional. Using the GGA functional in conjunction with the on-site corrections, we obtain a realistic picture of the bonding behavior and an accurate cohesive energy and cell volume. We therefore assume the GGA+$U$ method to be superior to GGA only because it reproduces best the electronic structure as well as the structural parameters at low computational costs. Tests, however, showed that the differences in energy barriers are in the range of $\approx 0.1$ eV when compared with GGA calculations. Unfortunately, it is presently not possible to test the absolute accuracy of the exchange-correlation functional for barrier calculations in a bulk system such as $In_2O_3$.

Beside the exchange-correlation functional, the major errors can be expected to emerge from the finite cell size. Since

the Madelung-type electrostatic finite-size contributions cancel for defect migration, the energies are expected to converge more rapidly and scale like $1/N$ or faster (elastic interactions), where $N$ is the number of atoms. Due to the large number barriers and the fact that several different cell sizes are needed in order to evaluate the scaling behavior we have not investigated the cell size dependence, presently. Assuming that the cell-size effect is mainly caused by elastic strain fields the calculated values should be seen as an upper boundary for the migration energies in the diluted limit. We assume that the relative change in migration energies would be small when compared with the errors on an absolute scale. Therefore, the qualitative conclusions should not be affected by finite-size effects. It is also noteworthy that semilocal functionals tend to underestimate the energy barriers,[35,36] which may lead to fortious cancellations in our study.

## VI. SUMMARY AND CONLCUSION

For the oxygen vacancy and interstitials, we have shown that the break of symmetry and the omission of anion sites compared with the fluorite lattice introduces migration barriers with considerably low energies. However, these barriers can only contribute to the prefactor at relevant temperatures. The oxygen vacancy diffusion is mediated by two of the four nearest oxygen neighbors plus one process to the second neighborhood. For the interstitials we have found diffusion to occur via a mixed interstitial/interstitialcy mechanisms. The regular interstitial mechanism connects interstitial sites along $\langle 111 \rangle$ axis whereas jumps away from the $\langle 111 \rangle$ axis need to proceed via an interstitialcy mechanism for indium as well as oxygen interstitials, where the multiplicity is higher for oxygen interstitials.

Migration is mediated by processes along $\langle 111 \rangle$ for the indium interstitials, whereas the perpendicular direction is rate determining for the oxygen interstitials. Indium vacancy diffusion is found to have energy barriers of about 2 eV. The diffusion mechanisms are such that the indium sites with higher symmetry are avoided most of the time. The lowest migration barrier can provide a complete path throughout the structure. Lastly, we have investigated oxygen dumbbell diffusion which occurs on the oxygen sublattice. We found that the normal interstitial positions are avoided in this case. The nearest neighbors do not significantly contribute to diffusion

of this defect. Dumbbell defects mainly perform on-site rotations and dumbbell exchange takes place along $\langle 110 \rangle$ directions within $\{111\}$ planes which are part of the second-neighbor shell. The symmetry is strongly broken and there is a whole ladder of possible transition energies. A strong charge state dependence is found for migrating oxygen rather than for indium atoms and is systematic for different migration processes.

We have presented a comprehensive study on diffusion mechanisms in indium oxide of the cubic polytype. It is an attempt to quantify the kinetics of point-defect migration in a C-type rare-earth crystal structure (bixbyite) by means of first-principles calculations. We have mapped out the total-energy surface in $In_2O_3$ for possible migration paths for several defects in their predominant charge states. We find a wealth of contributing migration processes, especially for defects which are bound to the oxygen sublattice ($V_O$ and $O_{i,db}$). For most of the defects, we have shown that the low-energy processes do not dominate the effective exponential factor, which is the measured quantity in experiments. We have consistently determined the effective parameters for diffusion by means of KMC simulations. The oxygen interstitial migration was found to have higher migration energy in accordance with experiments and a migration which is fundamentally distinct from that of the cation interstitials. The latter defects migrate quasi-one dimensionally along $\langle 111 \rangle$ axis, whereas for oxygen interstitial ($q=-2$) migration the determining processes are jumps perpendicular to the $\langle 111 \rangle$ axis. The indium vacancies have been found to migrate slower but a measurable mobility should be expected for experiments at higher temperatures. Finally, the calculated annealing temperature of $V_O^{\cdot\cdot}$ could be related to irreversible features in electrical conductivity measurements.

*Corresponding author: agoston@mm.tu-darmstadt.de

[1] H. L. Hartnagel, A. K. J. Dawar, and C. Jagadish, *Semiconducting Transparent Thin Films* (Institute of Physics, Bristol, 1995).

[2] I. Hamberg and C. G. Granqvist, J. Appl. Phys. **60**, R123 (1986).

[3] A. Klein, Appl. Phys. Lett. **77**, 2009 (2000).

[4] Y. Gassenbauer, R. Schafranek, A. Klein, S. Zafeiratos, M. Hävecker, A. Knop-Gericke, and R. Schlögl, Phys. Rev. B **73**, 245312 (2006).

[5] L. S. Hung and C. H. Chen, Mater. Sci. Eng. R **39**, 143 (2002).

[6] A. Walsh *et al.*, Phys. Rev. Lett. **100**, 167402 (2008).

[7] F. Fuchs and F. Bechstedt, Phys. Rev. B **77**, 155107 (2008).

[8] G. Frank and G. Köstlin, Appl. Phys. A **27**, 197 (1982).

[9] S. P. Harvey, T. O. Mason, Y. Gassenbauer, R. Schafranek, and A. Klein, J. Phys. D **39**, 3959 (2006).

[10] G. Rupprecht, Z. Phys. **139**, 504 (1954).

[11] J. H. W. de Wit, J. Solid State Chem. **13**, 192 (1975).

[12] S. Lany and A. Zunger, Phys. Rev. Lett. **98**, 045501 (2007).

[13] P. Ágoston, P. Erhart, A. Klein, and K. Albe, J. Phys.: Condens. Matter **21**, 455801 (2009).

[14] G. P. Wirtz and H. P. Takiar, J. Am. Ceram. Soc. **64**, 748 (1981).

[15] I. Ikuma and T. Murakami, J. Electrochem. Soc. **143**, 2698 (1996).

[16] Y. Ikuma, M. Kamiya, N. Okumura, I. Sakaguchi, H. Haneda, and Y. Sawada, J. Electrochem. Soc. **145**, 2910 (1998).

[17] G. Kresse and J. Furthmüller, Phys. Rev. B **54**, 11169 (1996).

[18] G. Kresse and J. Furthmüller, Comput. Mater. Sci. **6**, 15 (1996).

[19] P. E. Blöchl, Phys. Rev. B **50**, 17953 (1994).

[20] G. Kresse and D. Joubert, Phys. Rev. B **59**, 1758 (1999).

[21] J. P. Perdew, K. Burke, and M. Ernzerhof, Phys. Rev. Lett. **77**, 3865 (1996), erratum: **78**, 1396 (1997).

[22] S. L. Dudarev, G. A. Botton, S. Y. Savrasov, C. J. Humphreys, and A. P. Sutton, Phys. Rev. B **57**, 1505 (1998).

[23] P. Erhart, A. Klein, R. G. Egdell, and K. Albe, Phys. Rev. B **75**, 153205 (2007).

[24] G. Henkelman and H. Jónsson, J. Chem. Phys. **113**, 9978 (2000).

[25] G. Henkelman, B. P. Uberuaga, and H. Jónsson, J. Chem. Phys. **113**, 9901 (2000).

[26] G. H. Vineyard, J. Phys. Chem. Solids **3**, 121 (1957).

[27] R. L. Weiher, J. Appl. Phys. **33**, 2834 (1962).

[28] P. Ágoston and K. Albe, Phys. Chem. Chem. Phys. **11**, 3226 (2009).

[29] O. Warschkow, D. E. Ellis, G. B. González, and T. O. Mason, J. Am. Ceram. Soc. **86**, 1700 (2003).

[30] P. Ágoston, K. Albe, R. M. Nieminen, and M. J. Puska, Phys. Rev. Lett. **103**, 245501 (2009).

[31] Although the energy barriers do not differ much, we have found indications that the difference would increase for larger cell sizes.

[32] K. A. Fichthorn and W. H. Weinberg, J. Chem. Phys. **95**, 1090 (1991).

[33] This estimate is based on the Einstein equation and assumes the equilibration of a micrometer sized sample within an hour.

[34] C. Xirouchaki, G. Kiriakidis, T. F. Pedersen, and H. Fritzsche, J. Appl. Phys. **79**, 9349 (1996).

[35] J. Baker, M. Muir, and J. Andzelm, J. Chem. Phys. **102**, 2063 (1995).

[36] J. L. Durant, Chem. Phys. Lett. **256**, 595 (1996).